The prediction of broadband shock-associated noise including propagation effects

by

Steven A. E. Miller and Philip J. Morris

reprinted from

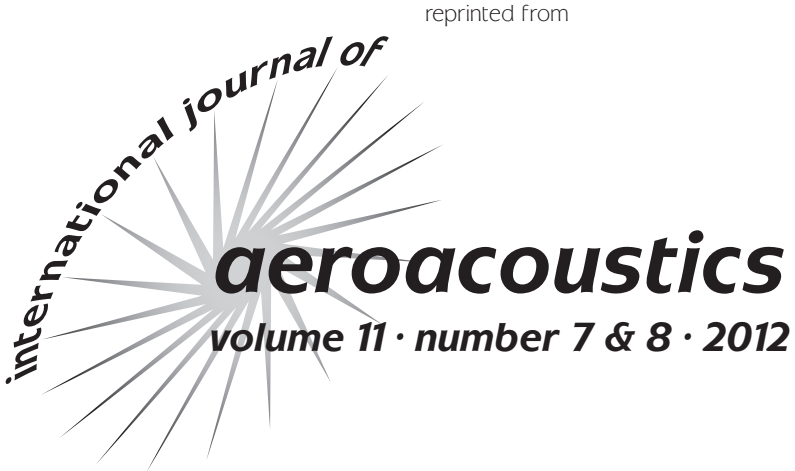

published by MULTI-SCIENCE PUBLISHING CO. LTD.,
5 Wates Way, Brentwood, Essex, CM15 9TB UK
E-MAIL: mscience@globalnet.co.uk
WEBSITE: www.multi-science.co.uk

International Journal of Aeroacoustics volume 11 · number 7 & 8 · 2012 – pages 755 – 781

The prediction of broadband shock-associated noise including propagation effects

Steven A. E. Miller and Philip J. Morris*

The National Aeronautics and Space Administration, Langley Research Center, 2 N. Dryden St. MS 461, Hampton, VA 23681

The Pennsylvania State University, Department of Aerospace Engineering, 233 Hammond Building, University Park, PA 16802

Submitted: Oct. 7, 2011; Revised: June 18, 2012; Accepted: July 18, 2012

ABSTRACT

An acoustic analogy is developed based on the Euler equations for broadband shock-associated noise (BBSAN) that directly incorporates the vector Green's function of the linearized Euler equations and a steady Reynolds-Averaged Navier-Stokes solution (SRANS) to describe the mean flow. The vector Green's function allows the BBSAN propagation through the jet shear layer to be determined. The large-scale coherent turbulence is modeled by two-point second order velocity cross-correlations. Turbulent length and time scales are related to the turbulent kinetic energy and dissipation rate. An adjoint vector Green's function solver is implemented to determine the vector Green's function based on a locally parallel mean flow at different streamwise locations. The newly developed acoustic analogy can be simplified to one that uses the Green's function associated with the Helmholtz equation, which is consistent with a previous formulation by the authors. A large number of predictions are generated using three different nozzles over a wide range of fully-expanded jet Mach numbers and jet stagnation temperatures. These predictions are compared with experimental data from multiple jet noise experimental facilities. In addition, two models for the so-called 'fine-scale' mixing noise are included in the comparisons. Improved BBSAN predictions are obtained relative to other models that do not include propagation effects.

Key words: Jet, Noise, Broadband, Shock, Propagation

PERSONAL INTRODUCTION (PJM)

It is an honor to be invited to contribute an article to this special edition in honor of Dr. J. M. (Jack) Seiner. The present paper concerns the predictions of broadband shock-associated noise (BBSAN). Jack made seminal contributions to the present understanding of BBSAN with his extensive experimental studies with his colleagues

*Corresponding author. Email addresses: s.miller@nasa.gov (Steven A. E. Miller), pjm@psu.edu (Philip J. Morris)

at NASA Langley Research Center - among others, Jim Yu, Tom Norum, Mike Ponton and Bernie Jansen. Under Jack's leadership this excellent team produced an extensive noise database that has provided guidance in the development of BBSAN models (see Tam and Tanna [1], Tam [2], Tam [3], and the present authors' contribution [4]). In addition, Jack's measurements provided the foundation for the concepts of the Large-Scale and Fine-Scale Similarity Spectra [5] and the different noise generation mechanisms associated with each of them. Last, and far from least, was Jack's commitment to research that would have a tangible beneficial effect on society and also provide support for the Armed Forces. To that end, Jack focused a great deal of attention in recent years on methods for the reduction of noise from high performance military aircraft engines. Jack and his colleagues conducted extensive model and flight tests. He also invented and patented a noise reduction concept based on removable corrugated seals [6]. This device reduced both BBSAN and mixing noise at take-off conditions.

At the later stages of his career, after moving from the NASA Langley Research Center to the University of Mississippi, Jack took on the daunting task of designing and building a new heated jet anechoic facility. As with everything to which Jack turned his hand, this facility is now one of the premier aeroacoustics research laboratories in the world.

Jack was a good friend and companion to me as well as many other researchers, old and young alike. He never held back from offering his opinion on your work or ideas - and he didn't always agree with your approach. But he would generally be correct, and you would have to be a fool not to listen carefully to his criticism, opinions and advice.

Jack and I shared many travels, beers, and fishing trips together. He was always fun to be around. But he didn't suffer fools gladly. The aeroacoustics community has lost a giant and a champion, and his presence is already being missed. Thank you Jack for all the good times.

1. INTRODUCTION

Broadband shock-associated noise (BBSAN) is present in supersonic jets when the jet is operating off-design. This occurs due to a difference between the static pressure at the nozzle exit and the ambient pressure. Nozzles that operate at the nominal on-design pressure ratio can also create a periodic shock cell structure in the jet plume if the characteristic waves are not canceled by the nozzle walls or the flow separates inside the nozzle. BBSAN occurs in nozzles that are both convergent or convergent-divergent when the flow is either over- or under-expanded. The interaction between the large-scale coherent turbulence in the jet shear layer and the shock cells is the source of shock-associated noise. BBSAN is observed in the far-field as a broad spectral peak and dominates the mixing noise levels at large angles from the downstream centerline axis. The peak frequency is a function of the jet shock cell spacing, the convection velocity of the jet shear layer turbulence, and observer location. The amplitude of BBSAN depends on the ratio of observer distance to the jet diameter, the polar and azimuthal observer angles, the geometry of the nozzle, the degree of off-design operation, and to a lesser degree, the stagnation temperature. The degree of off-design operation is represented by the off-design parameter, which is defined by $\beta = |M_j^2 - M_d^2|^{1/2}$. M_j is

the fully-expanded jet Mach number, which depends on the nozzle pressure ratio and the ratio of specific heats, and M_d is the nozzle design Mach number, which depends on the nozzle throat to exit area ratio.

Harper-Bourne and Fisher [7] performed one of the first investigations of BBSAN and developed the first prediction methodology for BBSAN. Their proposition was that BBSAN depends on the nearly coherent interaction between the turbulence in the jet shear layer and the jet's nearly periodic shock cell structure. This can be modeled as a series of correlated point sources that radiate either constructively or destructively. Harper-Bourne and Fisher's prediction scheme depends on knowledge of the rate of decay of the turbulence correlation between shocks, as well as the characteristic spectral shape of the radiated noise generated by each interaction. These were obtained using a least squares procedure to match the model with experimental noise measurements. The method is used in the SAE ARP876 [8] prediction method for single stream shock-associated noise from convergent nozzles at supercritical conditions and is included as a prediction module in NASA's Aircraft Noise Prediction Program (ANOPP) [9]. Harper-Bourne and Fisher's model [7] predicted the peak frequency of BBSAN as a function of observer angle, convective Mach number, and shock cell spacing.

Tam [2] developed a different method for BBSAN prediction. The basic physical model is described by Tam and Tanna [1]. Tam argued that the shock cell structure in the jet could be modeled, following the work of Pack [10], as a waveguide, where the waves are forced by the pressure imbalance at the jet exit and are confined by the jet shear layer. The simplest model that can be used for the jet is a vortex sheet. The effects of the slow divergence of the jet and the dissipative effects of the turbulence on the shock cells can also be included in the same general framework as shown by Tam *et al*. [11] The large-scale turbulence in the jet shear layer is modeled as a random superposition of instability waves supported by the jet mean flow, as described by Tam and Chen [12]. The interaction between the downstream traveling instability waves and the nearly periodic shock cell structure results in an interference pattern of traveling waves. The phase velocity of these waves can be higher than that of the instability waves alone and gives rise to noise radiation at large angles to the jet downstream axis, including the upstream direction. Since there is a random set of instability waves interacting with the shock cells, the resulting radiation pattern involves broad lobes rather than a sharply directional radiation. Empirical formulas are used to represent the shock cell spacing, the convection velocity of the turbulence, and the spectral width of the measured noise data. The predictions give good agreement with noise measurements in both the jet's near- and far-fields and certain key features of the measured spectra are captured. These include the variation of the frequency of the broadband spectral peak with observer location (the same formula obtained by the Harper-Bourne and Fisher [7] model), the narrowing of the width of the noise spectrum as the observer moves towards the jet upstream direction, and the presence of multiple lobes in the near-field and far-field noise spectra.

Tam [3] modified the model by Tam [2] to include the prediction of BBSAN from heated jets up to a moderate off-design parameter. This was accomplished by better

approximating the shock cell spacing and strength. A temperature correction factor, T'_{cf} was included to correct the over-prediction at all frequencies that occurred with increasing total temperature ratio (TTR). Another important modification was the use of different scaling factors that were dependent on whether the jet was over- or under-expanded.

Morris and Miller [4] developed a prediction method for BBSAN that uses a RANS CFD solution for the properties of the flow-field. Sources are modeled using dimensional arguments that scale as the shock pressure, turbulent velocity fluctuations, and an integral length scale of turbulence in the jet shear layer. The cross-correlation of the jet turbulence is modeled in a separable form, as first suggested by Ribner [13], which scales with the turbulent kinetic energy. The final closed form model equation is a volume integral over the jet plume and a single integral of the shock cell pressure wavenumber spectrum. All the quantities in the closed form model equation can be found based on a steady Reynolds-Averaged Navier-Stokes (SRANS) solution. Simple models relate the turbulence quantities to the SRANS solution.

The model by Morris and Miller [4] has been applied to dualstream and rectangular jets by Miller and Morris [14]. This work demonstrated the first BBSAN predictions of dualstream jets using an acoustic analogy. However, the approximation that the mean flow has negligible effect on the noise is not appropriate for dualstream jets if the dominant shock noise is from interactions between the primary shear layer turbulence and the shock cells. This is due to the refraction effects of the secondary stream shear layer. Miller and Morris [14] also demonstrated the first rectangular nozzle BBSAN predictions based on SRANS solutions. The developed model equation makes no assumption regarding the geometry of the nozzle and is not limited to rectangular or circular geometries.

Kuo *et al*. [15] performed experimental studies of various jets operating at off-design conditions and various total temperature ratios. The effects of these variations in temperature were compared to the far-field spectra in an attempt to find scaling laws of BBSAN. A simple empirical model was constructed to fit individual spectral shapes at various operating conditions. As with the model of Tam [2], the BBSAN spectra are chosen to consist of Gaussian-like peaks. Recently Viswanathan *et al*. [16] measured the saturation of BBSAN with stagnation temperature and separated the turbulent mixing noise from the BBSAN.

In the present paper an acoustic analogy is developed that is based on the Euler equations for the prediction of BBSAN. The propagation is addressed through the use of the vector Green's function to the linearized Euler equations as a component of the solution to the acoustic analogy. Any adjoint vector Green's function solver for the linearized Euler equations could be used in the solution. In the present work the vector Green's function is found numerically by using a locally parallel flow assumption that is similar to the approach of Tam and Auriault [17], Raizada [18], and Khavaran *et al*. [19]. Predictions using the newly developed BBSAN model are compared with the previous model by Morris and Miller [4] and experimental data from the National Aeronautics and Space Administration (NASA), the Pennsylvania State University (PSU), and the Boeing Company.

In addition to the prediction of BBSAN, the prediction of so-called 'fine-scale' mixing noise is also performed. The fine-scale mixing noise component radiates in all directions from the jet but is overshadowed by the noise from large-scale structures in the downstream direction and partially by the BBSAN in the sideline directions. It occurs at all jet Mach numbers. In the present paper the fine-scale mixing noise models of Tam and Auriault [20] and Morris and Boluriaan [21] are used. These fine-scale mixing noise models are simple to implement in the developed computer code RANS Integration for Shock Noise (RISN) due to their modular nature and the similar arguments used by the BBSAN model. The fine-scale mixing noise models use the same form of the vector Green's function that are used in the new BBSAN model described below. The combination of fine-scale mixing and BBSAN predictions yields a partial prediction of the total noise created by off-design supersonic heated jets. However, it should be noted that no model is included for the large-scale mixing noise in the peak noise radiation direction.

The next section describes the development of the new BBSAN prediction model in detail. Details regarding the implementation of the BBSAN model in RISN are given. The determination of the various parameters in the models and the evaluation of the models themselves are then described. Extensive predictions are performed using the RISN code and comparisons are made with experimental data. A wide range of design Mach numbers and operating conditions are selected to compare the predictions with experiment. Finally, conclusions are drawn based on the comparisons between the BBSAN predictions and measurements.

2. PHYSICAL AND MATHEMATICAL BBSAN MODEL

Mean flow effects in the BBSAN model of Morris and Miller [4] are neglected, and an approximation of the vector Green's function of the linearized Euler equations is used. This involves assuming that the vector Green's function for the linearized Euler equations is related to the Green's function of the Helmholtz equation, which does not include mean flow effects. In the present paper, the vector Green's function of the linearized Euler equations is determined from the solutions to Lilley's equation. It can be shown that the present model, when the previous simplified form of the vector Green's functions is inserted, reduces to the model originally developed by Morris and Miller [4]. The new prediction method has the same advantages as the previous model, but takes into account the mean flow effects that are present and particularly important in dualstream jets.

A vector Green's function solver for the linearized Euler equations is required to complete the newly developed prediction model. Tam and Auriault [20] and Karabasov *et al*. [22] have developed a three-dimensional adjoint solver for the linearized Euler equations for a general mean flow. However, here, a simpler approach is adopted by the authors that is based on a locally parallel flow approximation. Tam and Auriault [17] examined mean flow refraction effects for sound radiation from jets using parallel and diverging mean flows. They found that outside the cone of silence the parallel flow assumption yields highly accurate solutions relative to the diverging jet solution. Care

must be taken when interpreting refraction effects when the observer is within the cone of silence. At each streamwise location of the jet, mean flow properties are extracted from the SRANS solution to calculate the Green's function of Lilley's equation. This is obtained from a numerical solution of a single differential equation. As shown below, the Green's function of Lilley's equation can be used to calculate the vector Green's function of the linearized Euler equations. This step is performed at each streamwise location for each observer angle and frequency.

The governing equations chosen to form the acoustic analogy are the Euler equations. This is similar to the approach developed by Tam [2]. Tam's analysis is considerably simplified if the following form of the inviscid compressible equations of motion are used,

$$\frac{D\pi}{Dt} + \frac{\partial v_i}{\partial x_i} = 0 \tag{1}$$

$$\frac{Dv_i}{Dt} + c^2 \frac{\partial \pi}{\partial x_i} = 0 \tag{2}$$

where D is the material derivative, c is the local speed of sound, t is time, and v_i are the velocity components in the x_i directions of a Cartesian coordinate system. π is related to the logarithm of the pressure,

$$\pi = \frac{1}{\gamma} \ln \left(p / p_\infty \right) \tag{3}$$

where p is the pressure, p_∞ is the ambient pressure, and γ is the ratio of specific heats of an ideal gas.

Following Tam [2], the instantaneous flow-field properties are separated into four components. That is,

$$\begin{bmatrix} \pi \\ v_i \end{bmatrix} = \begin{bmatrix} \overline{\pi} + \pi_s + \pi_t + \pi' \\ \overline{v}_i + v_{si} + v_{ti} + v_i' \end{bmatrix} \tag{4}$$

where the overbar denotes the long time averaged value, the subscript s denotes the perturbations associated with the shock cell structure, the subscript t denotes the fluctuations associated with the turbulence, and the primes denote the fluctuations generated by the interaction of the turbulence and the shock cell structure. It is assumed that the shock cell structure satisfies the steady linearized version of Eqns. 1 and 2. In addition, it is assumed that the unsteady linearized version of these equations is also satisfied by the turbulent velocity fluctuations. This is justified if the important components of the turbulence, so far as the broadband shock-associated noise is concerned, are coherent over relatively large axial distances. These components are described well by a linear instability wave model.

Making these assumptions, the inhomogeneous equations for the fluctuations associated with the interaction of the turbulence with the shock cells can be written,

$$\frac{\partial \pi'}{\partial t} + \overline{v}_j \frac{\partial \pi'}{\partial x_j} + \frac{\partial v_i'}{\partial x_i} = \theta \tag{5}$$

$$\frac{\partial v_i'}{\partial t} + \overline{v}_j \frac{\partial v_i'}{\partial x_j} + v_j' \frac{\partial \overline{v}_i}{\partial x_j} + \overline{c}^2 \frac{\partial \pi'}{\partial x_i} = f_i^v + f_i^a \tag{6}$$

The terms on the left hand side of Eqns. 5 and 6 are the linearized Euler equations in terms of the perturbation quantities π' and v_i'. The terms that appear on the right hand sides represent the equivalent sources of the BBSAN. They are defined by,

$$\theta = -v_{sj} \frac{\partial \pi_t}{\partial x_j} - v_{tj} \frac{\partial \pi_s}{\partial x_j} \tag{7}$$

$$f_i^v = -v_{sj} \frac{\partial v_{ti}}{\partial x_j} - v_{tj} \frac{\partial v_{si}}{\partial x_j} \tag{8}$$

$$f_i^a = -c_s^2 \frac{\partial \pi_t}{\partial x_i} - c_t^2 \frac{\partial \pi_s}{\partial x_i} \tag{9}$$

where θ is a dilatation rate generated by the interaction between the pressure gradients and velocity perturbations of the turbulence and the shock cells. f_i^v is the unsteady force per unit volume associated with interactions between the turbulent velocity fluctuations and the velocity perturbations associated with the shock cells. Finally, f_i^a is the unsteady force per unit volume related to the interaction of fluctuations in the sound speed (or temperature), caused by the turbulence and the shock cells, and the associated pressure gradients. In traditional approaches to turbulent mixing noise models these equivalent sources have been treated separately and the same assumption is made here. The solution to Eqns. 5 and 6, can be written in terms of the vector Green's function that satisfies the equations,

$$\frac{\partial \pi_g^n}{\partial t} + \overline{v}_j \frac{\partial \pi_g^n}{\partial x_j} + \frac{\partial v_{gi}^n}{\partial x_i} = \delta(\underline{x} - \underline{y})\delta(t - \tau)\delta_{0n} \tag{10}$$

$$\frac{\partial v_{gi}^n}{\partial t} + \overline{v}_j \frac{\partial v_{gi}^n}{\partial x_j} + v_{gj}^n \frac{\partial \overline{v}_i}{\partial x_j} + \overline{c}^2 \frac{\partial \pi_g^n}{\partial x_i} = \delta(\underline{x} - \underline{y})\delta(t - \tau)\delta_{in} \tag{11}$$

where $\pi_g^n = \pi_g^n(\underline{x}, \underline{y}, t-\tau)$ and $v_{gi}^n = v_{gi}^n(\underline{x}, \underline{y}, t-\tau)$ are the components of the vector Green's function, equivalent to π' and v_i' in the general homogeneous problem. $\underline{x}$ denotes the observer position, $\underline{y}$ denotes the source location, $\delta(\ )$ is the Dirac delta function, and τ is the source emission time. δ_{ij} is the Kronecker delta function. For small perturbation pressures, $\pi' \simeq p'/\gamma p_\infty = p'/\rho_\infty c_\infty^2$. Then the solution for the pressure $p'(\underline{x}, t)$ can be written,

$$\begin{aligned} p'(\underline{x},t) = \rho_\infty c_\infty^2 \int_{-\infty}^{\infty}\int_{-\infty}^{\infty}\int_{-\infty}^{\infty}\int_{-\infty}^{\infty} \Big\{ \pi_g^0(\underline{x},\underline{y},t-\tau)\theta(\underline{y},\tau) \\ + \sum_{n=1}^{3} \pi_g^n(\underline{x},\underline{y},t-\tau)[f_n^v + f_n^a](\underline{y},\tau) \Big\} d\tau d\underline{y} \end{aligned} \tag{12}$$

The periodic Green's function is also introduced, given by,

$$\pi_g^n(\underline{x},\underline{y},\omega) = \int_{-\infty}^{\infty} \pi_g^n(\underline{x},\underline{y},t-\tau)\exp[-i\omega(t-\tau)]dt \tag{13}$$

$$\pi_g^n(\underline{x},\underline{y},t-\tau) = \frac{1}{2\pi}\int_{-\infty}^{\infty} \pi_g^n(\underline{x},\underline{y},\omega)\exp[i\omega(t-\tau)]d\omega \tag{14}$$

From this point, only the source term associated with the velocity perturbations will be considered. It is expected that the scaling of the other source terms would be similar. The exception would be the source term associated with the temperature fluctuations. However, the importance of this term still remains the subject of debate in the prediction of turbulent mixing noise in heated jets. So, this term will not be considered further. Then, the pressure fluctuation is given by,

$$p'(\underline{x},t) = \frac{\rho_\infty c_\infty^2}{2\pi}\int_{-\infty}^{\infty}\cdots\int_{-\infty}^{\infty}\left\{\sum_{n=1}^{3}\pi_g^n(\underline{x},\underline{y},\omega)f_n^v(\underline{y},\tau)\right\}\exp[i\omega(t-\tau)]d\omega d\tau d\underline{y} \tag{15}$$

Now the autocorrelation of the pressure can be formed. It is given by,

$$\begin{aligned} \overline{p'(\underline{x},t)p'(\underline{x},t+\tau^*)} = \frac{\rho_\infty^2 c_\infty^4}{(2\pi)^2}\int_{-\infty}^{\infty}\cdots\int_{-\infty}^{\infty}\left\{\sum_{n=1}^{3}\sum_{m=1}^{3}\right. \\ \left.\times\, \pi_g^n(\underline{x},\underline{y},\omega_1)\pi_g^m(\underline{x},\underline{z},\omega_2)\overline{f_n^v(\underline{y},\tau_1)f_m^v(\underline{z},\tau_2)}\right\} \\ \times \exp[i\omega_1(t-\tau_1) + i\omega_2(t-\tau_2) + i\omega\tau^*]d\omega_1 d\omega_2 d\tau_1 d\tau_2 d\underline{y} d\underline{z} \end{aligned} \tag{16}$$

The spectral density is given by the Fourier transform of the autocorrelation of the pressure,

$$S(\underline{x},\omega)=\int_{-\infty}^{\infty}\overline{p'(\underline{x},t)p'(\underline{x},t+\tau^{*})}\exp(-i\omega\tau^{*})d\tau^{*} \tag{17}$$

The integration with respect to τ^{*} can be performed immediately.

Before proceeding it is necessary to examine the form of the two-point cross-correlation of f_v^n. It is dependent on the strength of the shock cells and the turbulent fluctuations and its product is significant in regions where the shocks and expansions intersect with the turbulent shear layer. The amplitude of f_v^n will be proportional to the shock cell pressure perturbations and the turbulent velocity fluctuations. It is assumed that the two-point cross-correlation function of the BBSAN source term can be written in terms of separation distance $\underline{\eta}=\underline{z}-\underline{y}$ and separation time $\tau=\tau_2-\tau_1$. Then, following integrations with respect to τ_1,ω_1 and ω_2, we can write,

$$\begin{aligned}S(\underline{\mathrm{x}},\omega)=\rho_\infty^2c_\infty^4\int_{-\infty}^{\infty}\cdots\int_{-\infty}^{\infty}\Bigg\{\sum_{n=1}^{3}\sum_{m=1}^{3}\pi_g^n(\underline{\mathrm{x}},\underline{\mathrm{y}},-\omega)\,\pi_g^m(\underline{\mathrm{x}},\underline{\mathrm{y}},+\underline{\eta},\omega)\\ \times R_{nm}^v(\underline{\mathrm{y}},\underline{\eta},\tau)\Bigg\}\exp[-i\omega\tau]d\tau d\underline{\eta}d\underline{\mathrm{y}}\end{aligned} \tag{18}$$

where R_{nm}^v is the two-point cross-correlation of the equivalent source term f_n^v,

$$R_{nm}^v(\underline{\mathrm{y}},\underline{\eta},\tau)=\overline{f_n^v(\underline{\mathrm{y}},t)f_m^v(\underline{\mathrm{y}}+\underline{\eta},t+\tau)}. \tag{19}$$

The SRANS solution does not provide any information about the form of f_n^v, so a model for R_{nm}^v is constructed as,

$$R_{nm}^v(\underline{\mathrm{y}},\underline{\eta},\tau)=\frac{1}{\rho_\infty^2c_\infty^2l^2}\,p_s(\underline{\mathrm{y}})p_s(\underline{\mathrm{y}}+\underline{\eta})R_{mn}(\underline{y},\underline{\eta},\tau) \tag{20}$$

where R_{nm} is the two-point cross correlation function of the turbulent velocity fluctuations in the n and m directions and l is a characteristic length scale in the axial direction. Over the distance where the spatial correlation is significant we assume that,

$$\pi_g^m(\underline{x},\underline{y}+\underline{\eta},\omega)=\pi_g^m(\underline{x},\underline{\mathrm{y}},\omega)\exp\left[i\frac{\omega}{c_\infty}\frac{\underline{x}}{x}\cdot\underline{\eta}\right] \tag{21}$$

as argued by Tam and Auriault [17]. Also, from the definition of π_g^m,

$$\pi_g^n(\underline{x},\underline{y},-\omega)=\pi_g^{n^*}(\underline{x},\underline{y},\omega) \tag{22}$$

where the asterisk denotes a complex conjugate. Then,

$$S(\underline{\mathrm{x}},\omega)=c_\infty^2\int_{-\infty}^{\infty}\cdots\int_{-\infty}^{\infty}\left\{\sum_{n=1}^{3}\sum_{m=1}^{3}\pi_g^{n^*}(\underline{\mathrm{x}},\underline{\mathrm{y}},\omega)\,\pi_g^{m}(\underline{\mathrm{x}},\underline{\mathrm{y}},\omega)\frac{p_s(\underline{\mathrm{y}})p_s(\underline{\mathrm{y}}+\underline{\eta})}{l^2}\right.$$
$$\left.\times R_{nm}(\underline{\mathrm{y}},\underline{\eta},\tau)\right\}\exp\left[-i\omega\left(\tau-\frac{\underline{x}\cdot\underline{\eta}}{c_\infty x}\right)\right]d\tau d\underline{\eta}d\underline{\mathrm{y}} \tag{23}$$

One of the shock cell pressure distributions is now represented in terms of its axial wavenumber spectrum,

$$\tilde{p}_s(k_1,y_2,y_3)=\int_{-\infty}^{\infty}p_s(\underline{\mathrm{y}})\exp[ik_1y_1]dy_1 \tag{24}$$

and the corresponding inverse Fourier transform is,

$$p_s(\underline{\mathrm{y}})=\frac{1}{2\pi}\int_{-\infty}^{\infty}\tilde{p}_s(k_1,y_2,y_3)\exp[-ik_1y_1]dk_1 \tag{25}$$

Then,

$$S(\underline{\mathrm{x}},\omega)=\frac{c_\infty^2}{2\pi}\int_{-\infty}^{\infty}\cdots\int_{-\infty}^{\infty}\left\{\sum_{n=1}^{3}\sum_{m=1}^{3}\pi_g^{n^*}(\underline{\mathrm{x}},\underline{\mathrm{y}},\omega)\,\pi_g^{m}(\underline{\mathrm{x}},\underline{\mathrm{y}},\omega)\right.$$
$$\left.\times\frac{p_s(\underline{\mathrm{y}})\tilde{p}_s(k_1,y_2+\eta,y_3+\zeta)}{l^2}R_{nm}(\underline{\mathrm{y}},\underline{\eta},\tau)\right\} \tag{26}$$
$$\times\exp[-ik_1\xi]\exp\left[-i\omega\left(\tau-\frac{\underline{x}\cdot\underline{\eta}}{c_\infty x}\right)\right]dk_1d\tau d\underline{\eta}d\underline{\mathrm{y}}$$

Now, we introduce the wavenumber frequency spectrum of the turbulent velocity fluctuations. That is,

$$S_{nm}(\underline{\mathrm{y}},\underline{k}^*,\omega^*)=\int_{-\infty}^{\infty}\cdots\int_{-\infty}^{\infty}R_{nm}(\underline{\mathrm{y}},\underline{\eta},\tau)\exp[-i(\omega^*\tau-\underline{k}^*\cdot\underline{\eta})]d\underline{\eta}d\tau \tag{27}$$

With

$$R_{nm}(\underline{y},\underline{\eta},\tau)=\frac{1}{(2\pi)^4}\int_{-\infty}^{\infty}\cdots\int_{-\infty}^{\infty}S_{nm}(\underline{\mathrm{y}},\underline{k}^*,\omega^*)\exp[i(\omega^*\tau-\underline{k}^*\cdot\underline{\eta})]d\underline{k}^*d\omega^* \tag{28}$$

In Morris and Miller [4] it was assumed that the shock cell structure was independent of the cross-stream distance over the distance where R_{nm} remained significant. From an examination of the wavenumber spectrum as a function of r, this appears to be a reasonable assumption. Obviously, in the azimuthal direction for axisymmetric jets this is also true. So, we can replace $\tilde{p}_s(k_1, y_2 + \eta, y_3 + \zeta)$ by $\tilde{p}_s(k_1, y_2, y_3)$ as before. Then the integrations with respect to τ, ω^*, $\underline{\eta}$, and $\underline{k}^*$ can be performed. This gives,

$$S(\underline{x},\omega) = \frac{c_\infty^2}{2\pi}\int_{-\infty}^{\infty}\cdots\int_{-\infty}^{\infty}\left\{\sum_{n=1}^{3}\sum_{m=1}^{3}\pi_g^{n^*}(\underline{x},\underline{y},\omega)\,\pi_g^{m}(\underline{x},\underline{y},\omega)\right.$$
$$\left.\times\frac{p_s(\underline{y})\tilde{p}_s(k_1,y_2,y_3)}{l^2}S_{nm}\left[\underline{y},\left(\frac{\omega x_1}{c_\infty x}-k_1\right),\frac{\omega x_2}{c_\infty x},\frac{\omega x_3}{c_\infty x},\omega\right]\right\}dk_1 d\underline{y} \tag{29}$$

In Eqn. 29 the wavenumber frequency spectrum of the turbulent velocity fluctuations is to be evaluated at an axial wavenumber $k_1^* = (\omega x_1/c_\infty x - k_1)$. In turn, the axial wavenumber spectrum of the shock cell structure will be dominated by bands centered around wavenumbers corresponding to the fundamental shock cell spacing and its harmonics. This includes both positive and negative axial wavenumbers. The peak amplitude of the turbulent velocity wavenumber frequency spectrum will occur close to where $k_1^* = \omega/u_c$, where u_c is the convection velocity of the turbulence. Thus the peak frequency in the radiated noise spectrum will vary as,

$$\frac{\omega\cos\theta}{c_\infty} - k \simeq \frac{\omega}{u_c}. \tag{30}$$

This gives a peak frequency variation of,

$$f = \frac{u_c}{L}\frac{1}{(1 - M_c\cos\theta)}, \tag{31}$$

where L is the fundamental shock cell wavelength or spacing and $M_c = u_c/c_\infty$. It should be noted that because of the sign convention used in the spatial Fourier transforms, the dominant noise contributions occur for negative values of k_1. Equation 31 is identical to the formula given by Harper-Bourne and Fisher [7] based on a coherent point source model and Tam and Tanna [1] based on an instability wave model.

Now, consider the form of the two-point cross-correlations of the velocity fluctuations. For simplicity it will be assumed that they all have the same shape, but the amplitude will vary depending on the component. This is consistent with the approach used by Karabasov *et al.* [23] for the fourth-order cross-correlations. It can be expressed as,

$$R_{nm}(\underline{y},\underline{\eta},\tau) = a_{nm} K R(\underline{\eta},\tau) \tag{32}$$

where K is the turbulent kinetic energy and a_{nm} reflects the relative amplitudes of the different components of the second-order cross-correlation. The form chosen for $R(\underline{\eta}\,,\,\tau)$ is the same as used before by Morris and Miller [4]. That is,

$$R(\underline{\eta},\tau) = \exp[-\,|\,\tau\,|\,/\tau_s]\exp[-(\xi - u_c\tau)^2/l^2]\exp[-(\eta^2+\zeta^2)\,/\,l_\perp^2] \tag{33}$$

where it is assumed that the convection velocity is approximated well by the local mean velocity in regions of large values of *K*. From the definition of $S_{nm}(\underline{y},\,\underline{k}^*,\,\omega)$ given by Eqn. 27 it can be shown that,

$$S_{nm}(\underline{y},\underline{k}^*,\omega) = 2\pi^{3/2} a_{nm} K l l_\perp^2 \tau_s \frac{\exp\left\{-\left[k_1^{*2} l^2 + (k_2^{*2}+k_3^{*2})\,l_\perp^2\right]/\,4\right\}}{\left[1+(\omega - k_1^*\overline{u})^2\tau_s^2\right]} \tag{34}$$

Setting $\underline{x} = x$ (cos θ, sin θ cos ϕ, sin θ sin ϕ) the spectral density can be shown to be given by,

$$\begin{aligned} S(\underline{\mathrm{x}},\omega) = \pi^{1/2} c_\infty^2 \int_{-\infty}^{\infty}\cdots\int_{-\infty}^{\infty} \Bigg\{ \sum_{n=1}^{3}\sum_{m=1}^{3} \pi_g^{n^*}(\underline{\mathrm{x}},\underline{\mathrm{y}},\omega)\pi_g^{m}(\underline{\mathrm{x}},\underline{\mathrm{y}},\omega) \\ \times p_s(\underline{\mathrm{y}})\tilde{p}_s(k_1,y_2,y_3)\frac{a_{nm}Kl_\perp^2\tau_s}{l}\Bigg\} \\ \times \frac{\exp[-l^2(\omega\cos\theta\,/\,c_\infty - k_1)^2\,/\,4 - \omega^2 l_\perp^2\sin^2\theta\,/\,(4c_\infty^2)]}{[1+(1-M_c\cos\theta + \overline{u}k_1\,/\,\omega)^2\omega^2\tau_s^2]}\,dk_1\,d\underline{y} \end{aligned} \tag{35}$$

Equation 35 represents an acoustic analogy based on the Euler equations that uses the vector Green's function of the linearized Euler equations to predict BBSAN. Appendix A shows that this expression reduces to the result by Morris and Miller [4] when the vector Green's function based on the Helmholtz equation and an isotropic source model are used.

Evaluation of Eqn. 35 requires knowledge of the vector Green's function of the linearized Euler equations. An adjoint approach is followed here which shortens the calculation time greatly. This approach is based on the work of Tam and Auriault [17] and Raizada [18]. Assuming a locally parallel mean flow, $q = q(y,\,z)$, where q represents the field-variables, the adjoint Green's function can be written,

$$g_a(\underline{x},\underline{y},\omega) = \frac{\exp[-i\omega(x_1\cos\theta - R)\,/\,c_\infty]}{8\pi^2 c_\infty^2 R\omega}\sum_{m=0}^{\infty} f_m(r)\cos(m\phi) \tag{36}$$

where m is an azimuthal mode number. Equation 36 is valid inside the jet ($r < R_o$). There is no concern about solutions outside the jet as sources of BBSAN do not exist in that region. The quantity f_m is found for each mode m by solving the following differential equation in the region $0 < r < R_o$,

$$\frac{\partial^2 f_m}{\partial r^2} + \left[\frac{-4\cos\theta\,\frac{d\overline{u}}{dr}/c_\infty}{1-\overline{u}\cos\theta\,/c_\infty} - \frac{1}{\overline{\rho}}\frac{d\overline{\rho}}{dr} + \frac{1}{r}\right]\frac{\partial f_m}{\partial r} + \left[\frac{\omega^2\left(1-\frac{\overline{u}\cos\theta}{c_\infty}\right)}{\gamma p\,/\,\rho} + \frac{3\left(\frac{1}{\rho}\frac{d\overline{\rho}}{dr}\frac{d\overline{u}}{dr} - \frac{\partial^2\overline{u}}{\partial r^2}\right)\frac{\cos\theta}{c_\infty}}{1-\overline{u}\cos\theta/c_\infty} - \frac{m^2}{r^2} - \frac{\omega^2\cos^2\theta}{c_\infty^2}\right] f_m = 0 \tag{37}$$

As shown by Tam and Auriault [17], the solution near the centerline ($r \simeq \epsilon$) is $f_m = a_m r^m$. Using this expression, the boundary conditions at the centerline of the jet are specified and a spatial marching problem in the radial direction can be formed at each streamwise location. The details of the marching methods used are discussed in the next section. For each radial mode m, f_m needs to be scaled so that the inner-solution matches the outer-solution of g_a at $r = R_o$. Raizada [18] showed that the scaling factor is given by,

$$a_m = \frac{(-i)^m \epsilon_m \lambda\left(J_m(\lambda R_o)H_m^{(1)'}(\lambda R_o) - J_m'(\lambda R_o)H_m^{(1)}(\lambda R_o)\right)}{\lambda f_m(R_o)H_m^{(1)'}(\lambda R_o) - f_m'(R_o)H_m^{(1)}(\lambda R_o)} \tag{38}$$

where $\epsilon_m = 1$ for $m = 1$ and $\epsilon_m = 2$ for all other values of m. $\lambda = \omega \sin\theta/c_\infty$, and the primes denote a derivative of the Hankel function or f_m with respect to their arguments. The vector Green's function of the linearized Euler equations is related to the Green's function of Lilley's equation, $g\,(\underline{x},\,\underline{y}\,,\,\omega)$, by,

$$\pi_g^0 = \omega^2 g - 2i\overline{u}\omega\frac{\partial g}{\partial y_x} - \overline{u}^2\frac{\partial^2 g}{\partial y_x^2} \tag{39}$$

$$\pi_g^1(\underline{x},\underline{y},\omega) = -\left(i\omega + \overline{u}\frac{\partial}{\partial y_x}\right)\frac{\partial}{\partial y_x}\,g(\underline{\mathrm{x}},\underline{\mathrm{y}},\omega) \tag{40}$$

$$\pi_g^2(\underline{x},\underline{y},\omega) = -\left\{3\frac{d\overline{u}}{dy_r}\frac{\partial}{\partial y_x} - \left(i\omega + \overline{u}\frac{\partial}{\partial y_x}\right)\frac{\partial}{\partial y_r}\right\} g(\underline{\mathrm{x}},\underline{\mathrm{y}},\omega) \tag{41}$$

$$\pi_g^3(\underline{x},\underline{y},\omega) = -\left(i\omega + \overline{u}\frac{\partial}{\partial y_x}\right)\frac{1}{y_r}\frac{\partial}{y_\theta}\,g(\underline{\mathrm{x}},\underline{\mathrm{y}},\omega) \tag{42}$$

where $\underline{y} = (y_r, y_\theta, y_x)$ denotes the source position in cylindrical polar coordinates. The reciprocal relation of $g = g_a$ holds true for this formulation of the adjoint Green's function. Equations 39 through 42 require various terms involving derivatives of the Green's function to Lilley's equation. These expressions are found analytically based on the numerical calculation of g. The various derivatives of g used in Eqns. 39 through 42 with respect to the various spatial directions are,

$$\frac{\partial g}{\partial x} = \frac{-i\cos\theta}{8\pi^2 c_\infty^3 R}\exp[-i\omega(x\cos\theta - R)/c_\infty]\sum_{m=0}^{\infty} f_m(r)\cos(m\phi) \tag{43}$$

$$\frac{\partial^2 g}{\partial x^2} = \frac{-\omega\cos^2\theta}{8\pi^2 c_\infty^4 R}\exp[-i\omega(x\cos\theta - R)/c_\infty]\sum_{m=0}^{\infty} f_m(r)\cos(m\phi) \tag{44}$$

$$\frac{\partial g}{\partial \phi} = \frac{-m}{8\pi^2 \omega c_\infty^2 R}\exp[-i\omega(x\cos\theta - R)/c_\infty]\sum_{m=0}^{\infty} f_m(r)\sin(m\phi) \tag{45}$$

$$\frac{\partial}{\partial x}\left(\frac{1}{r}\frac{\partial g}{\partial \phi}\right) = \frac{im\cos\theta}{8r\pi^2 c_\infty^3 R}\exp[-i\omega(x\cos\theta - R)/c_\infty]\sum_{m=0}^{\infty} f_m(r)\sin(m\phi) \tag{46}$$

Equations 43 through 46 are used with Eqns. 39 through 42 to find the components of the required vector Green's function at different streamwise locations. Equations 39 through 42 and their corresponding complex conjugates can be used in the evaluation of Eqn. 35.

3. IMPLEMENTATION

The mathematical model developed in the previous section is implemented in the computer program RANS Integration for Shock Noise (RISN). RISN is a collection of jet noise prediction models that are based on various acoustic analogies and is being developed at NASA Langley Research Center (LaRC). The several prediction methodologies allow total noise predictions based on a summation of jet noise components from axisymmetric or three dimensional jet flowfields that are heated, off-design, and compressible. Acoustic analogies are developed for each noise source (eg: BBSAN, fine - and large-scale mixing noise, screech, etc.) and the sources and propagation are treated separately.

The implementation of the model in the absence of propagation effects is described fully in Morris and Miller [4]. The model developed in the present paper is implemented using the same strategy but with an additional subroutine to calculate the vector Green's functions. The model Eqn. 35 is evaluated for each observer position $\underline{x}$. This involves an integration over the sources of BBSAN in the jet plume. That is, where the turbulence is interacting with the oblique shock waves in the shear

layer. The range of integration in the streamwise direction (for single stream jets) is generally taken to extend from the nozzle exit to the end of the potential core and in the cross-stream direction from the centerline axis through twice the nozzle diameter. The integral associated with the axial wavenumber k_1, is performed by using the trapezoidal rule. Only peaks of $\widetilde{p}_s$ are included in the numerical integration as small values of $\widetilde{p}_s$ have negligible contribution to the magnitude of BBSAN. This is accomplished by integrating from the main peak of $\widetilde{p}_s$ to typically half the range of $\widetilde{p}_s$ over both negative and positive wavenumbers.

It is important to note that one of the assumptions in the formulation of the adjoint vector Green's function solver is that the static pressure everywhere in the jet is equal to the ambient. This assumption is necessary in order to form a single second order differential equation for the pressure from the Euler equations. This assumption is valid for all subsonic jets and on-design supersonic jets. Off-design supersonic jets have a shock cell structure due to the static pressure at the nozzle exit not matching the ambient static pressure. The resultant shocks and Prandtl-Meyer expansions cause the static pressure to be either greater or much smaller than the ambient values. However, the BBSAN sources exist near the outside of the jet in the shear layer and the pressure mismatch at these locations is very small. The sources of fine-scale mixing noise exist in the high speed shear layer, the transition region, and the fully developed region of the jet and are much more affected by this assumption.

The new prediction model and other associated models in RISN require knowledge of a mean flow. The mean flows are determined from solutions of the Steady Reynolds-Averaged Navier-Stokes equations (SRANS). The SRANS solutions are found using the NPARC Alliance Wind-US solver. Wind-US was developed by the NPARC Alliance which is a partnership between NASA Glenn Research Center (GRC), the U. S. Air Force Arnold Engineering Development Center, and additional contributors. Solutions from Wind-US are found using the default options of the CFD solver. The SRANS equations are closed by the Menter [24] shear stress transport (SST) turbulence model.

The fine-scale mixing noise models of Tam and Aurialt [20] and Morris and Boluriaan [21] have been implemented in the computer program RISN. These models provide predictions for the fine-scale turbulent mixing noise and are similar to or based on acoustic analogies. These models are simple to implement due in part to the modular design of the RISN code and the large number of arguments that are similar to those of the BBSAN models. Both models consist of spatial integrals that involve mean flow components, turbulence statistics based on the mean flow, and g_a or π_g^n. In the model of Tam and Auriault [20] the Green's function is based on the parallel flow assumption and is the same Green's function of Eqn. 36. The model of Morris and Boluriaan [21] uses the components of the vector Green's function of the linearized Euler equations shown as Eqns. 39 and 40. The vector Green's function of the linearized Euler equations is required for the evaluation of the developed prediction model for BBSAN in Eqn. 35. Thus, it is simple to include these mixing noise models as additional calculations in the RISN code as two additional subroutines.

4. RESULTS

This section presents predictions using the BBSAN and fine-scale mixing noise models. First, a description of the nozzles is given. The operating conditions for the nozzles are then shown. The CFD solutions for these nozzles operating over a range of conditions is discussed. Finally, noise predictions are compared with experimental data.

A number of nozzle geometries and operating conditions have been selected. The convergent nozzle developed by NASA, shown in Fig. 1, has an exit diameter of 0.0508 meters and is chosen to test a wide range of conditions. A convergent-divergent nozzle, shown in Fig. 2, designed at the Pennsylvania State University, is also selected. It has a design Mach number of 1.50 and an exit diameter of 0.0127 meters. This nozzle and associated experimental data are courtesy of Professor D. K. McLaughlin of the Pennsylvania State University. Finally, a dualstream nozzle, shown in Fig. 3, with convergent primary (core) and secondary (fan) streams is selected with primary nozzle exit diameter of 0.0622 meters, secondary nozzle exit inner diameter of 0.1017 meters,

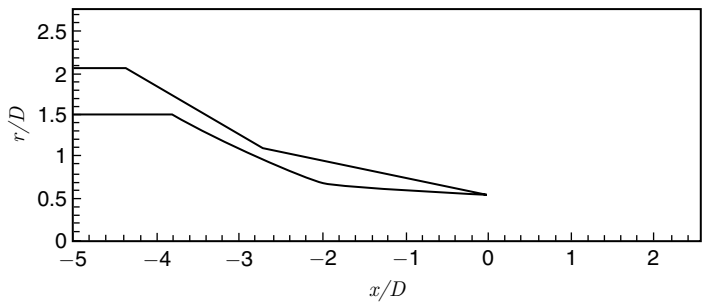

Figure 1: The nozzle contour of the singlestream convergent NASA nozzle. $D = 0.0508$ m.

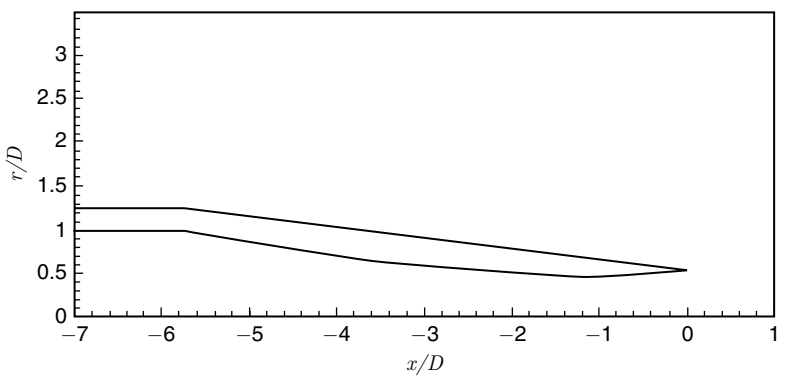

Figure 2: The nozzle contour of the singlestream convergent-divergent PSU nozzle. $D = 0.0127$ m.

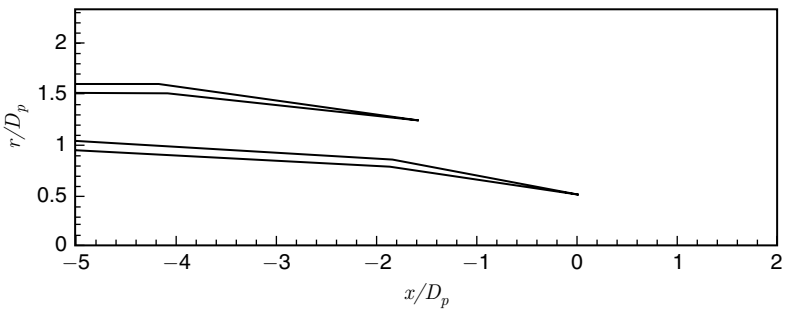

Figure 3: The nozzle contour of the dual stream nozzle. The core nozzle exit diameter is, $D_p = 0.0622$ m, the fan nozzle exit inner diameter is 0.101716 m, and fan nozzle exit outer diameter, $D_s = 0.15248$ m.

and outer diameter of 0.1525 meters. The dualstream nozzle exits are off-set axially. The secondary stream exit is 0.0984 meters upstream of the primary nozzle exit. This dualstream Boeing nozzle is selected to help illustrate the effect of the high speed secondary stream on the primary stream's BBSAN sources. This nozzle geometry and associated experimental data are courtesy of Dr. K. Viswanathan of the Boeing Company.

The nozzle operating conditions are summarized in Table 1 for single stream jets and Table 2 for dualstream jets. The first column describes the nozzle used and has an associated run number as a suffix. For each case there are corresponding nozzle pressure ratio (NPR) and total temperature ratio (TTR) values as well as the fully expanded Mach number M_j. The subscript p denotes the value for the primary flow or core nozzle and the subscript s denotes the operating condition of the secondary stream or fan flow.

Table 1: Nozzle operating conditions for single stream jets.

Nozzle	M_d	NPR	M_j	TTR
NASA	1.00	1.893	1.00	1.00
NASA	1.00	2.556	1.24	1.00
NASA	1.00	3.154	1.39	1.00
NASA	1.00	1.893	1.00	2.70
NASA	1.00	2.556	1.24	2.70
NASA	1.00	3.154	1.39	2.70
NASA	1.00	1.893	1.00	3.20
NASA	1.00	2.556	1.24	3.20
NASA	1.00	3.154	1.39	3.20
PSU	1.50	2.770	1.30	1.00
PSU	1.50	4.930	1.70	1.00
PSU	1.50	2.770	1.30	2.20
PSU	1.50	4.930	1.70	2.20

Table 2: Nozzle operating conditions for dual stream jets.

Nozzle	$M_{dp,ds}$	NPR_p	M_{jp}	TTR_p	NPR_s	M_{js}	TTR_s
Boeing	1.00	1.400	0.710	2.14	2.140	1.358	1.00
Boeing	1.00	2.700	1.281	2.87	2.870	0.848	1.00
Boeing	1.00	2.556	1.281	2.87	2.870	1.358	1.00

These cases are selected based on available experimental data and represent a wide range of over- and under-expanded conditions. In addition, a wide range of TTR are chosen to examine temperature effects on the noise predictions. SRANS solutions are produced by the Wind-US 2.0 solver for each case shown in Tables 1 and 2. The models have been exercised on each case. Only select cases are presented in this paper but are representative of the results for the cases not shown.

A single result is chosen to illustrate the SRANS solutions of each case from Tables 1 and 2. Figure 4 shows the Boeing Company nozzle operating at $NPR_p = 2.40$, $TTR_p = 2.70$, $M_{jp} = 1.192$, $NPR_s = 1.80$, $TTR_s = 1.00$, and $M_{js} = 0.959$. Contours of Mach number are shown. Both the core and fan nozzles are convergent, thus either stream can operate on-design, under-expanded, or subsonically. The shock cell structure can faintly be seen in the core stream and is contained by the high speed subsonic fan flow.

Before showing the jet noise predictions the format of their presentation is discussed. The predictions of the two BBSAN models and the two mixing noise models are shown in Figs. 5 through 8. Each figure shows a comparison of jet noise predictions with corresponding experimental data for a particular nozzle and the corresponding operating condition summarized in Tables 1 and 2. The formats of each figure are similar. For example, in Fig. 5 there are six sets of spectra shown and each one represents a different observer position. Observer positions are at one hundred

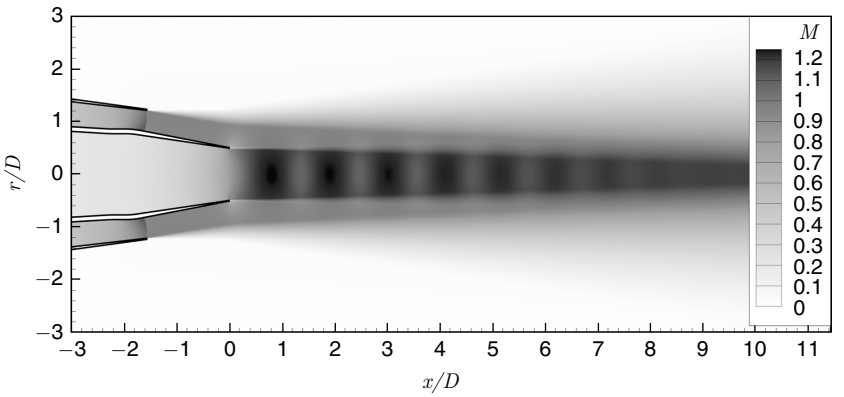

Figure 4: Mach number contour plot of the dualstream nozzle. The primary flow is under-expanded and supersonic operating at $M_j = 1.192$ and $TTR = 2.70$ and the secondary flow is operating at $M_j = 0.959$ and $TTR = 1.00$.

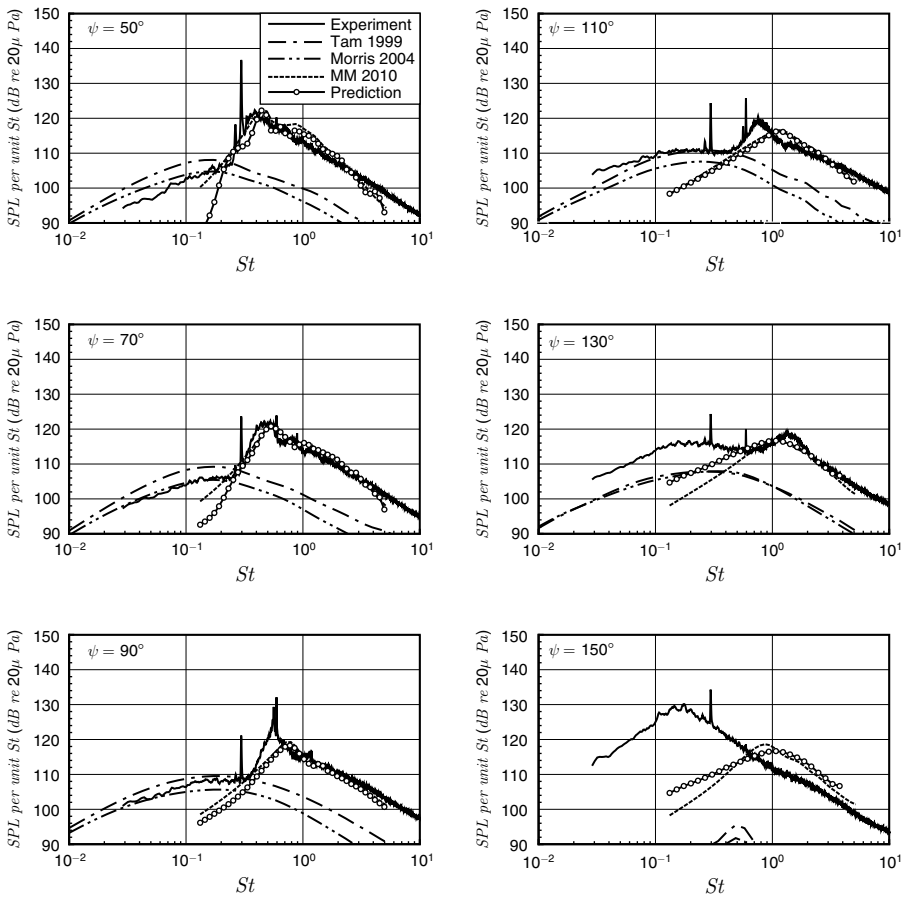

Figure 5: The noise spectra from the NASA nozzle, $M_d = 1.00$, $D = 0.0508$ m, with operating conditions $M_j = 1.39$ and $TTR = 1.00$, at a distance of $R/D = 100$ and observer angles Ψ.

nozzle diameters from the primary nozzle exit at inlet angles, Ψ, shown in the upper left hand corner. The downstream direction is represented by values of Ψ greater than ninety degrees. The frequency is non-dimensional in the form of the Strouhal number, St, using the fully expanded jet velocity u_j and the fully expanded diameter D_j. D_j is a nozzle exit diameter that provides an on-design flow based on a given throat diameter and NPR. Each set of experimental data is shown by a thin black line, the fine-scale mixing noise predictions of Tam and Auriault [20] are a long dash dot line, the fine-scale mixing noise predictions of Morris and Boluriaan [21] are a double dot dash line, the BBSAN predictions using Eqn. 51 (see Appendix A) are a dotted line and labeled as Morris and Miller 2010 (MM 2010), and the new BBSAN model

predictions Eqn. 35 are shown as thick black lines with white circles (labeled Prediction). Predictions of the noise produced by the large-scale coherent turbulence are not included in this study. The noise from the large-scale turbulent structures dominate the spectra in the downstream direction. In this direction it is expected that the predictions of BBSAN and fine-scale mixing noise will be much lower than the total SPL measured by experiment.

Fig. 5 shows results for the convergent NASA nozzle operating with a fully expanded Mach number of $M_j = 1.39$ and $TTR = 1.00$. At the sideline location in Fig. 5 the differences between the two BBSAN models are relatively small. This is due to the negligible effects that the shear layer has on the BBSAN propagating in the sideline direction. By examining the differences between the predictions of the two BBSAN models at various angles other than the sideline location, the effects of the mean flow on the BBSAN can be observed. In the upstream direction, the half-width of the main BBSAN peak is narrower and generally has a higher rate of decay at lower St when mean flow effects are included. However, this is a relatively small effect in the single jet case. This can be observed best at angles $\psi = 50$ and $\psi = 70$ degrees. In the downstream direction the opposite is true and the BBSAN decays at a lower rate away from the peak frequency when mean flow effects are included. At the sideline location the fine-scale mixing effects generally scale well with the experimental data. At the highest M_j the fine-scale predictions agree much better compared with the sonic case. Generally both fine-scale mixing noise predictions over-estimate the fine-scale mixing noise in the sideline and upstream directions. In the downstream direction the large-scale mixing noise dominates the fine-scale mixing noise. There is little variation in the fine scale mixing noise peak level predictions with observer angle. However, the measured mixing noise levels have increased considerably from $\psi = 130$ degrees to 150 degrees, indicating the dominance of the large-scale mixing noise at these downstream angles.

A second case is examined using the NASA nozzle shown in Fig. 6. The nozzle operates with $M_j = 1.24$ and $TTR = 3.20$. Relative to the previous single stream case there is substantial heating. This heating removes the strong screech tones present in the cold case. At the sideline location the effects of the meanflow on the shock noise predictions are minimal. The two predictions of BBSAN are almost identical. In the upstream direction predictions of BBSAN are also very similar. Differences are again apparent in the downstream direction, especially in the peak noise direction. It is difficult to know which predictions are more accurate in the peak noise direction because of the dominance of the large-scale mixing noise. At $\psi = 110$ degrees a small increase in the experimental result is observed at $St = 1.5$. This small increase is due to the BBSAN. Interestingly, the new prediction model finds this small increase over the mixing noise while the BBSAN prediction of Morris and Miller [4] under predict this contribution. The mixing noise predictions, like the predictions of BBSAN, have the same general spectral shape in the sideline and upstream directions. Only in the downstream directions do they differ significantly from the measurements, as expected.

The Penn State convergent-divergent nozzle has a design Mach number of 1.50 and exit diameter of 0.0127 m. The predictions at $\psi = 50$ degrees are not shown because

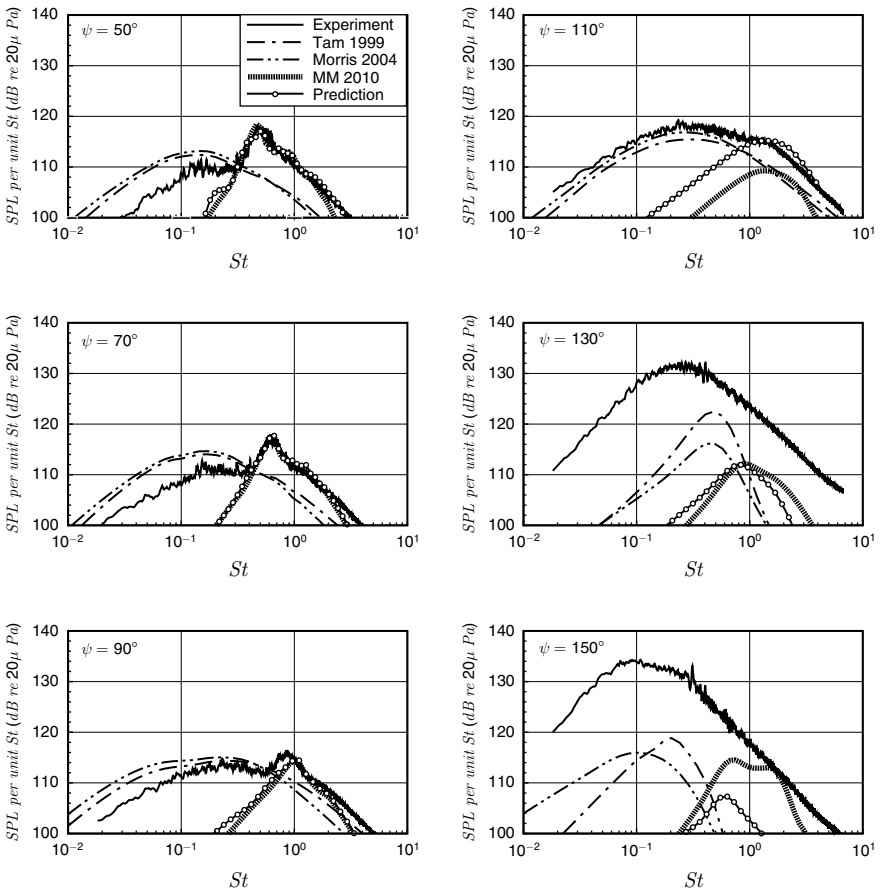

Figure 6: The noise spectra from the NASA nozzle, $M_d = 1.00$, $D = 0.0508$ m, with operating conditions $M_j = 1.24$ and $TTR = 3.20$, at a distance of $R/D = 100$ and observer angles Ψ.

experimental data is not available at this location. This final single stream case is shown in Fig. 7 for $M_j = 1.7$ and $TTR = 1.0$. In the upstream direction the BBSAN peak is narrower. In the downstream direction, the BBSAN predictions with mean flow effects are highly damped. This is best illustrated at an observer angle of $\psi = 150$ degrees. Screech tones typically lower the peak BBSAN frequency and raise its amplitude at the sideline location, which is generally free from mean flow propagation effects. The fine-scale turbulent mixing noise in the unheated and heated cases under-predict the experiment. In the unheated case the Tam and Auriault [20] model has better agreement with the experiment than that of Morris and Boluriaan [21].

The predictions and experimental spectra of one of the dualstream jet cases are now examined. Both the core and fan nozzles are convergent as shown in Fig. 3. The Boeing

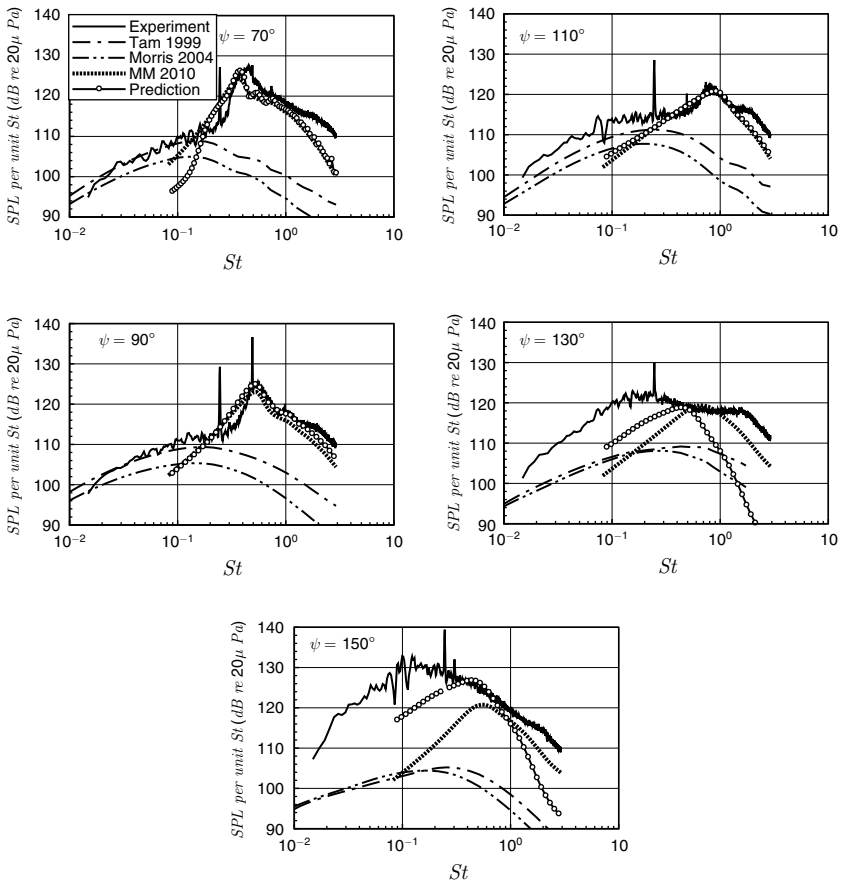

Figure 7: The noise spectra from the PSU nozzle, $M_d = 1.50$, $D = 0.0127$ m, with operating conditions $M_j = 1.70$ and $TTR = 1.00$, at a distance of $R/D = 100$ and observer angles Ψ. The experimental data is courtesy of Professor D. K. McLaughlin of the Pennsylvania State University.

dualstream nozzle operates at $M_{jp} = 1.281$, $M_{js} = 1.358$, $TTR_p = 2.870$, and $TTR_s = 1.00$ and the noise spectra are shown in Fig. 8. At the sideline location the predictions of Eqn. 35 and Eqn. 51 show slightly better agreement relative to the experimental magnitude and a much richer spectral content. Multiple BBSAN peaks can be seen at the higher BBSAN harmonics. In the downstream direction similar results are seen compared to previous BBSAN predictions relative to experimental data. The data in the upstream direction, particularly at $\psi = 50$ degrees, represents an important result of the present paper. The BBSAN predictions of Eqn. 35 show much improved agreement with experiment compared to the prediction of Eqn. 51. The predicted spectrum that includes the vector Green's function has much richer spectral content, a more accurate fall-off at low and high frequencies, and better amplitude agreement until $St = 2$.

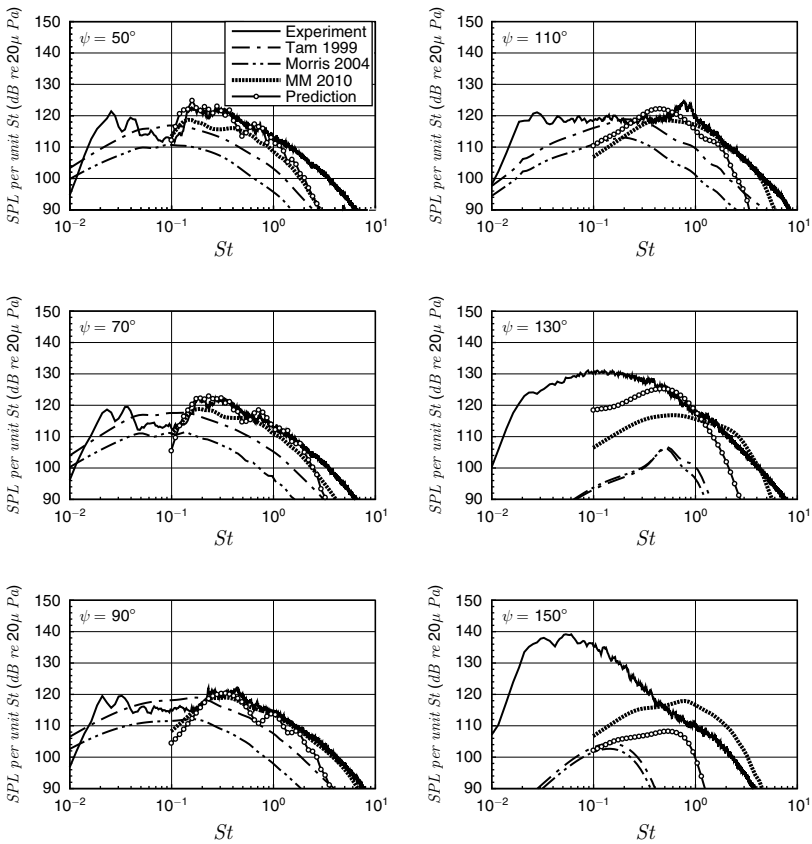

Figure 8: The noise spectra from the Boeing nozzle, $M_{dp} = 1.00$ $D_p = 0.06223$ m, $M_{ds} = 1.00$, $D_{si} = 0.1017$, m $D_{so} = 0.1525$ m, with operating conditions $M_{jp} = 1.281$, $M_{js} = 1.358$ and $TTR_p = 2.870$, $TTR_s = 1.00$, at a distance of $R/D = 100$ and observer angles Ψ. The experimental data is courtesy of Dr. K. Viswanathan of the Boeing Company.

5. CONCLUSION

An acoustic analogy based on the Euler equations has been formed for BBSAN. The parameter values for the model are provided by a steady mean flow solution of the RANS equations and the vector Green's function of the linearized Euler equations using an adjoint approach. This acoustic analogy reduces to the model developed by Morris and Miller [4] if the vector Green's function of the linearized Euler equations for a quiescent environment is used. Comparison of these two models shows that at the sideline location the spectral shape is the same. Thus, as expected, the mean flow effects are minimal if the observer is at the sideline location of the jet. In the downstream region, the mean flow effects on BBSAN generally decrease the noise levels. In the upstream direction the mean flow effects have more significance and the new BBSAN model shows better agreement

with experimental data than predictions that neglect mean flow effects. The newly developed model predictions show an increased number of broadband peaks, slightly better agreement in amplitude relative to experimental results, faster decay at lower frequencies and slower decay at higher frequencies relative to the peak frequency. These mean flow effects, although slight, generally yield more accurate predictions relative to the model of Morris and Miller [4]. In particular, the BBSAN calculations for the dualstream jets in the upstream direction show the most improvement.

The modular nature of RISN and the locally parallel adjoint vector Green's solver for the linearized Euler equations allowed implementation of the fine-scale mixing noise models of Tam and Auriault [20] and Morris and Boluriaan [21] with ease. In general the fine-scale turbulent mixing noise models capture the peak frequencies, peak amplitudes, and fall-off at high frequencies. At lower frequencies the models generally had too slow a spectral fall-off relative to experimental data. This could easily be corrected with changes described in the appendix of Morris and Boluriaan [21]. In the downstream direction the fine-scale mixing noise is dominated by the large-scale mixing noise. Thus, the fine-scale mixing noise models have little contribution to the total noise in the downstream direction.

The developed acoustic analogies for BBSAN and fine-scale mixing noise make use of a vector Green's function. The arguments of these models could easily be found by a numerical adjoint vector Green's function solver that makes no assumption about the flow-field or the geometry. In fact, use of a tailored vector Green's function could include the effects of reflections from the airframe and refraction due to the jet shear layer, without further modification to the acoustic analogies.

ACKNOWLEDGEMENTS

This research represents an informal collaboration between The National Aeronautics and Space Administration (NASA) Langley Research Center (LaRC) and The Pennsylvania State University. The first author is grateful for continuous support from the NASA Fundamental Aeronautics Program (FAP) High Sprrd Project. The authors are grateful for the experimental data provided by Dr. K. Viswanathan of the Boeing Company, Professor Dennis K. McLaughlin of the Pennsylvania State University, and the jet noise group of NASA Glenn Research Center at Lewis Field.

REFERENCES

[1] C. K. W. Tam, H. K. Tanna, Shock-Associated Noise of Supersonic Jets from Convergent-Divergent Nozzles, J. Sound Vib. 81 (3) (1982) 337–358.

[2] C. K. W. Tam, Stochastic model Theory of Broadband Shock-Associated Noise from Supersonic Jets, Journal of Sound and Vibration (1987) 265–302.

[3] C. K. W. Tam, Broadband Shock-Associated Noise of Moderately Imperfectly-Expanded Supersonic Jets, Journal of Sound and Vibration 140 (1) (1990) 55–71.

[4] P. J. Morris, S. A. E. Miller, Prediction of Broadband Shock-Associated Noise Using Reynolds-Averaged Navier-Stokes Computational Fluid Dynamics, AIAA Journal 48 (12) (2010) 2931–2961.

[5] C. K. W. Tam, M. Golebiowski, J. M. Seiner, On the Two Components of Turbulent Mixing Noise from Supersonic Jets, AIAA Paper 96–1716 (1996).

[6] J. M. Seiner, Method and Device for Reducing Engine Noise, United States Patent, US 7, 475, 550 B2 (January 2009).

[7] M. Harper-Bourne, M. J. Fisher, The Noise from Shock-Waves in Supersonic Jets, AGARD (1973).

[8] SAE International, SAE ARP876, Revision D. Gas Turbine Jet Exhaust Noise Prediction, SAE International, Warrendale, PA, 1994.

[9] W. E. Zorumski, Aircraft Noise Prediction Program. Theoretical manual. Parts 1 and 2, NASA TM 83199 (1982).

[10] D. C. Pack, A note on Prandtls Formula for the Wavelength of a Supersonic Gas Jet, Quarterly Journal of Applied Mathematics and Mechanics 3 (1950) 173–181.

[11] C. K. W. Tam, J. A. Jackson, J. M. Seiner, A Multiple-Scales Model of the Shock-Cell Structure of Imperfectly Expanded Supersonic Jets, Journal of Fluid Mechanics 153 (1985) 123–149.

[12] C. K. W. Tam, K. C. Chen, A Statistical Model of Turbulence in Two-Dimensional Mixing Layers, Journal of Fluid Mechanics 92 (1979) 303–326.

[13] H. S. Ribner, The Generation of Sound by Turbulent Jets, Advances in Applied Mechanics 8 (1964) 104–182.

[14] S. A. E. Miller, P. J. Morris, The Prediction of Broadband Shock-Associated Noise from Dualstream and Rectangular Jets Using RANS CFD, 16th AIAA/CEAS Aeroacoustics Conference AIAA 2010–3730.

[15] C. Kuo, D. K. McLaughlin, P. J. Morris, Effects of Supersonic Jet Conditions on Broadband Shock-Associated Noise, 49th AIAA Aerospace Sciences Meeting including the New Horizons Forum and Aerospace Exposition AIAA 2011–1032.

[16] K. Viswanathan, M. B. Alkislar, M. J. Czech, Characteristics of the Shock Noise Component of Jet Noise, AIAA Journal 48 (1) (2010) 25–46.

[17] C. K. W. Tam, L. Auriault, Mean Flow Refraction Effects on Sound Radiated from Localized Sources in a Jet, Journal of Fluid Mechanics 370 (1998) 149–174.

[18] N. Raizada, Numerical Prediction of Noise from High Speed Subsonic Jets using an Acoustic Analogy, M. S. Thesis The Pennsylvania State University.

[19] A. Khavaran, J. Bridges, N. Georgiadis, Prediction of Turbulence-Generated Noise in Unheated Jets, NASA TM-2005-213827.

[20] C. K. W. Tam, L. Auriault, Jet Mixing Noise from Fine-Scale Turbulence, AIAA Journal 37 (2) (1999) 145–153.

[21] P. J. Morris, S. Boluriaan, The Prediction of Jet Noise From CFD Data, 10th AIAA/CEAS Aeroacoustics Conference.

[22] S. A. Karabasov, T. P. Hynes, A. P. Dowling, Effect of Mean-Flow Evolution on Sound Propagation through Non-Uniform Jet Flows, 13th AIAA/CEAS Aeroacoustics Conference AIAA-2007-3655.

[23] S. A. Karabasov, M. Z. Afsar, T. P. Hynes, A. P. Dowling, W. A. McMullan, C. D. Pokora, G. J. Page, J. J. McGuirk, Jet Noise: Acoustic Analogy Informed by Large Eddy Simulation, AIAA Journal 48 (7) (2010) 1312–1325.

[24] F. R. Menter, Two-Equation Eddy-Viscosity Turbulence Models for Engineering Applications, AIAA Journal 32 (8) (1994) 1598–1605.

[25] J. Proudman, The Generation of Noise by Isotropic Turbulence, Proc. Roy. Soc. A. 214 (119).

APPENDIX A

It is shown here that Eqn. 35 reduces to the model equation of Morris and Miller [4]. The mean flow effects are neglected by using the Green's function of the Helmholtz equation. This can be performed by setting the mean flow conditions to their ambient values in Eqns. 10 and 11, taking the Fourier transform with respect to time, and finding the Green's function. This yields,

$$g(\underline{x},\underline{z},\omega)=\frac{-1}{4\pi\left|\underline{x}-\underline{z}\right|}\exp\left[-i\omega\left|\underline{x}-\underline{z}\right|/c_{\infty}\right] \tag{47}$$

where $\underline{z}$ is a vector to the source locations. Note that the sign of the exponent gives outgoing waves for the time variation implied by Eqn. 14. The vector Green's function of the linearized Euler equations for a quiescent environment based on Eqns. 10 and 11 is,

$$\begin{aligned}\pi_g^n(\underline{x},\underline{y},\omega)&=\frac{-\delta_{in}}{c_{\infty}^2}\int_{\underline{z}}\delta(\underline{z}-\underline{y})\frac{\partial}{\partial z_i}(g(\underline{x},\underline{y},\omega))d\underline{z}\\&-\frac{\delta_{0n}}{c_{\infty}^2}\int_{\underline{z}}g(\underline{x},\underline{z},\omega)\delta(\underline{z}-\underline{y})d\underline{z}\end{aligned} \tag{48}$$

Substituting Eqn. 47 into Eqn. 48, assuming that the observer is in the far-field, and simplifying the previous equation yields an expression for the vector Green's function in the absence of varying mean flow (which is very similar to the Green's function of the Helmholtz equation),

$$\pi_g^n\left(\underline{x},\underline{y},\omega\right)=\frac{i\omega x_n}{4\pi c_{\infty}^3x^2}\exp\left[-i\omega x/c_{\infty}\right]\delta_{in}+\frac{i\omega}{4\pi c_{\infty}^2x}\exp\left[-i\omega x/c_{\infty}\right]\delta_{0n} \tag{49}$$

Substituting Eqn. 49 into Eqn. 35 yields,

$$S\left(\underline{\mathrm{x}},\omega\right)=\frac{1}{16\pi^{3/2}c_{\infty}^{4}x^{2}}\int_{-\infty}^{\infty}\cdots\int_{-\infty}^{\infty}\sum_{n=1}^{3}\sum_{m=1}^{3}a_{nm}\frac{x_{n}x_{m}}{x^{2}}\omega^{2}$$
$$\times\frac{Kl_{\perp}^{2}\tau_{s}}{l}p_{s}\left(\underline{\mathrm{y}}\right)\tilde{p}_{s}\left(k_{1},y_{2},y_{3}\right)$$
$$\times\frac{\exp\left[-l^{2}\left(\omega\cos\theta/c_{\infty}-k_{1}\right)^{2}/4-\omega^{2}l_{\perp}^{2}\sin^{2}\theta/\left(4c_{\infty}^{2}\right)\right]}{1+\left(1-M_{c}\cos\theta+\overline{u}k_{1}/\omega\right)^{2}\omega^{2}\tau_{s}^{2}}dk_{1}d\underline{y} \tag{50}$$

This expression for the spectral density provides no account for the mean flow effects but retains the ability to specify anisotropic turbulence. Morris and Miller [4] used the Proudman [25] form for isotropic turbulence, $a_{nm}x_{n}x_{m}/x^{2}=2/3$. Using this assumption and simplifying yields,

$$S\left(\underline{\mathrm{x}},\omega\right)=\frac{1}{24\pi^{3/2}c_{\infty}^{4}x^{2}}\int_{-\infty}^{\infty}\cdots\int_{-\infty}^{\infty}\frac{Kl_{\perp}^{2}}{l\tau_{s}}p_{s}\left(\underline{\mathrm{y}}\right)\tilde{p}_{s}\left(k_{1},y_{2},y_{3}\right)$$
$$\times\tau_{s}^{2}\omega^{2}\frac{\exp\left[-l^{2}\left(\omega\cos\theta/c_{\infty-}k_{1}\right)^{2}/4-\omega^{2}l_{\perp}^{2}\sin^{2}\theta/\left(4c_{\infty}^{2}\right)\right]}{1+\left(1-M_{c}\cos\theta+\overline{u}k_{1}/\omega\right)^{2}\tau_{s}^{2}\omega^{2}}dk_{1}d\underline{y} \tag{51}$$

which is the model equation developed in Morris and Miller [4]. There are three minor differences. The first arises as a more consistent notation has been used in the present paper for the spatial and temporal Fourier transforms and their inverses. This changes the sign of k_1. However, since $\tilde{p}_s(k_1, y_2, y_3)$ is an even function of k_1 this does not change the result. The second minor difference is a factor of 2/3 that comes from the definition of a_{nm}. Eqn. 51 is applicable to three-dimensional flow-fields, but has the simplifications of isotropic turbulence and no effects of BBSAN propagation induced by variations of the shear layer mean flow. Finally, an incorrect factor of exp (ik_1y_1) has been removed.